

pubs.acs.org/JPCC Article

# Facile Fabrication of Composite Ag/Fe<sub>3</sub>O<sub>4</sub> and Porous Fe<sub>3</sub>O<sub>4</sub> Nanorods Based on Oblique Angle Codeposition

Weijie Huang, Xibo Li, Bin Ai,\* and Yiping Zhao



Cite This: J. Phys. Chem. C 2021, 125, 11750-11755



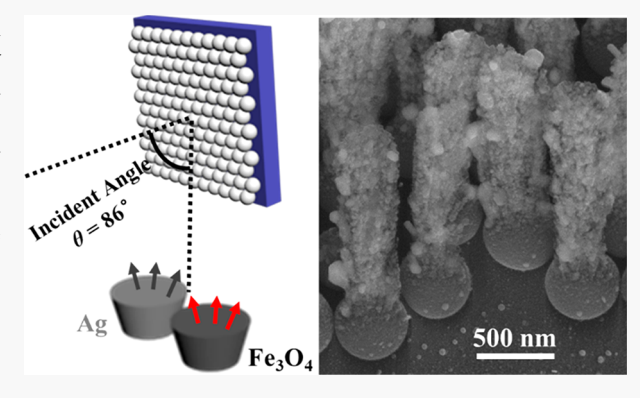
**ACCESS** 

III Metrics & More

Article Recommendations

Supporting Information

**ABSTRACT:** Composite  $Ag/Fe_3O_4$  and porous  $Fe_3O_4$  nanorods with controlled shape, size, composition, and porosity were fabricated by oblique angle codeposition as well as subsequent annealing and chemical etching. The codeposition supplies a way to evaporate two materials simultaneously to form composites, which would lead to a greater variety of nanorods. The composite  $Ag/Fe_3O_4$  and porous  $Fe_3O_4$  nanorods showed ferromagnetism, tunable optical properties, and strong carrier capability, which are believed to benefit the applications of biosensing, bioimaging, catalysis, targeted drug delivery, and therapeutic agent.



## **■ INTRODUCTION**

Fe<sub>3</sub>O<sub>4</sub> nanostructures (NSs) possess remarkable properties of low cost, low toxicity, and unique magnetism. They have recently become the most popularly used magnetic materials in various fields including biotechnology,2-4 biosensing,5 catalysis, magnetic fluids, separation techniques, energy storage,9,10 and environmental remedy.11 The performance of Fe<sub>3</sub>O<sub>4</sub> NSs is pertinently affected by their morphology, size, structure, and surface properties. For example, as carriers for targeted drug delivery, porous Fe<sub>3</sub>O<sub>4</sub> nanoparticles (NPs) are excellent due to their efficient delivery of theranostic agents and magnetic targeting ability. 12 Moreover, porous Fe<sub>3</sub>O<sub>4</sub> NPs could improve both the drug loading ratio and the therapeutic efficiency. 13 On the other hand, Fe<sub>3</sub>O<sub>4</sub> NPs doped with carbon significantly increased the conductivity when Fe<sub>3</sub>O<sub>4</sub> NPs were used for capacitor electrodes.<sup>14</sup> In addition, metal/Fe<sub>3</sub>O<sub>4</sub> composite NPs are particularly of interest because the metal surface can be easily functionalized with other small molecules, functional ligands, or biomolecules, 15-17 which could easily assemble multifunctional hybrid NSs for wide applications. In this regard, much attention has been focused on the development of efficient fabrication/synthesis approaches to produce shape-, size-, and composition-controlled Fe<sub>3</sub>O<sub>4</sub> NSs, especially porous and composite NSs. 18-20 Often composite Fe<sub>3</sub>O<sub>4</sub> NSs are mainly prepared via chemical synthesis processes, including coprecipitation, hydrothermal synthesis, thermal decomposition, sol-gel synthesis, sonochemical synthesis, microemulsion, electrochemical synthesis, electrospray synthesis, and bacterial and microorganism synthesis. 21,22 Complicated protocols and operations are required in these methods, while the shape, size, composition, etc., still cannot

be precisely controlled due to the uncertainty in chemical reaction processes. Facile and versatile preparation methods of composite and porous  ${\rm Fe_3O_4}$  NSs with desirable properties are in great demand.

In this work, composite Ag/Fe<sub>3</sub>O<sub>4</sub> nanorods (NRs) and porous Fe<sub>3</sub>O<sub>4</sub> NRs with controlled shape, size, and porosity were fabricated based on a simple and versatile oblique angle codeposition (OACD) technique. Ag and Fe<sub>3</sub>O<sub>4</sub> were codeposited at an incident angle of 86° onto SiO<sub>2</sub> nanosphere arrays, forming Ag-Fe<sub>2</sub>O<sub>3</sub>-Fe<sub>3</sub>O<sub>4</sub> composite NRs. After annealing, Fe<sub>2</sub>O<sub>3</sub> was transformed to Fe<sub>3</sub>O<sub>4</sub> and Ag/Fe<sub>3</sub>O<sub>4</sub> NRs were obtained. Ag was then selectively etched, generating porous Fe<sub>3</sub>O<sub>4</sub> NRs. During codeposition, by changing the relative deposition rates of the two materials, the composition of the resulting composite NSs can be tuned systematically. The magnetic and optical properties as well as the molecular adsorption capacity of the composite Ag/Fe<sub>3</sub>O<sub>4</sub> NRs and porous Fe<sub>3</sub>O<sub>4</sub> NRs show that composite Ag/Fe<sub>3</sub>O<sub>4</sub> nanorods (NRs) and porous Fe<sub>3</sub>O<sub>4</sub> NRs have great potential in catalysis, targeted drug delivery, and therapeutic agent.

# METHODS

Fabrication of Composite Ag/Fe<sub>3</sub>O<sub>4</sub> Nanorods. SiO<sub>2</sub> monolayers with diameters of 500 and 800 nm were prepared

 Received:
 March 30, 2021

 Revised:
 May 12, 2021

 Published:
 May 24, 2021





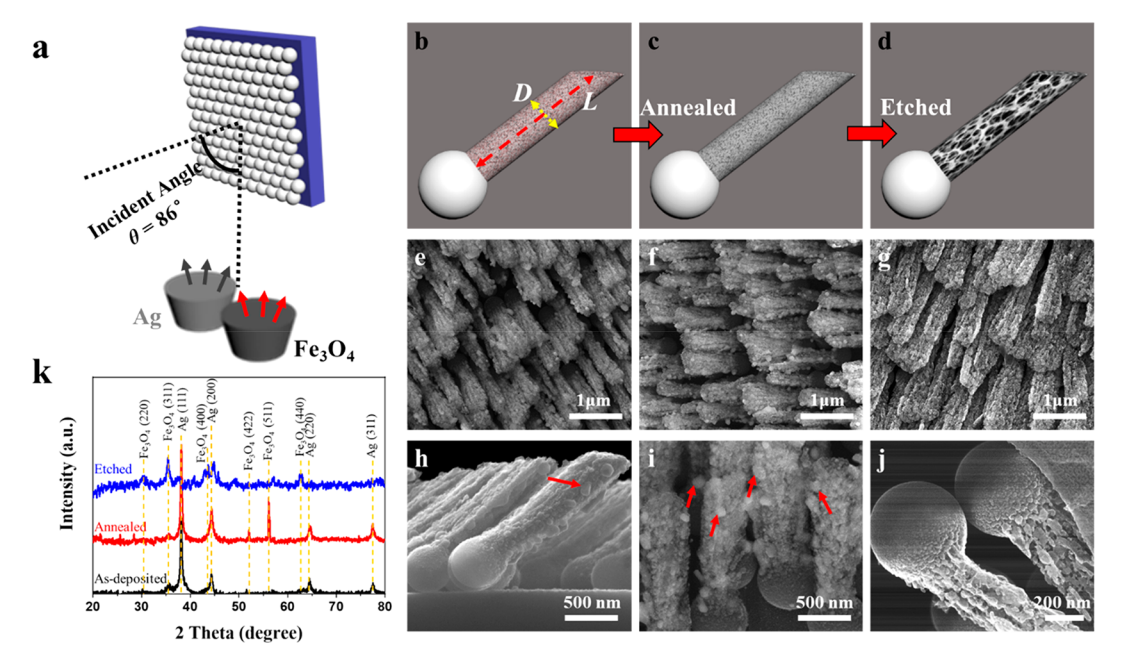


Figure 1. (a) Schematic of the fabrication configuration. (b-d) Material transformation processes from composite  $Ag/Fe_2O_3$  NRs to composite  $Ag/Fe_3O_4$  NRs and then to porous  $Fe_3O_4$  NRs. Representative SEM images of the (e, h) as-deposited samples, (f, i) composite  $Ag/Fe_3O_4$ , and (g, j) porous  $Fe_3O_4$  NRs. Red arrows indicate the Ag NPs on the surface of NRs. (k) XRD patterns of the as-deposited (black), annealed (composite  $Ag/Fe_3O_4$ , red), and etched (porous, blue) NRs.

on glass substrates using an air—water interface method as previously reported. The SiO $_2$  monolayers were then loaded in a custom-built dual-source electron deposition system (Pascal Technology), and the deposition configuration is shown in Figure 1a. The vapor incident angles of Ag and Fe $_3$ O $_4$  with respect to the substrate normal were 86°. The deposition chamber was pumped down to a base pressure of  $<1\times10^{-6}$  Torr. The deposition rate and total thickness of each evaporation source were monitored using two quartz crystal microbalances (QCM) independently while tuning the deposition rate  $R_{\rm Ag}$ : $R_{\rm Fe}_3$ O $_4$  = 1:2 and 1:1. The as-deposited samples were annealed in N $_2$ /EtOH at 350 °C for 1 h. Composite Ag/Fe $_3$ O $_4$  nanorods were formed.

**Fabrication of Porous Fe<sub>3</sub>O<sub>4</sub> Nanorods.** The samples after being annealed were then etched to remove Ag. The etchant solution used was 0.05 M KCN (Fisher Scientific, ACS grade) in 99.9% pure methanol (ACS grade) solvent. The samples were etched for different time durations of 1, 3, 5, 10, 15, 20, 40, and 50 min. All of these samples were etched by holding them using clamps with nanorods facing down in the etchant solution under magnetic stirring. Then, the samples were washed in distilled water and absolute ethanol several times to remove the impurities before characterization.

**Characterization.** The optical transmission spectra (T) were measured using an ultraviolet—visible spectrophotometer (UV-vis, Jasco-750). Extinction spectra were obtained according to the equation  $E = -\ln(T)$ . High-resolution scanning electron microscopy (SEM) was carried out using a Hitachi SU9000 STEM/SEM (Hitachi, Chatsworth, CA, USA) at 30 kV equipped with an Oxford solid state EDS detector (Oxford Instruments, Concord, MA, USA). The crystal structures were characterized using a PANalytical X'Pert PRO MRD X-ray diffractometer (XRD) with a fixed incidence angle of  $0.5^{\circ}$ . The field dependence of magnetization was measured by a vibrating sample magnetometer (VSM, model EZ7; MicroSense, LLC).

# ■ RESULTS AND DISCUSSION

Ag/Fe<sub>3</sub>O<sub>4</sub> NRs were fabricated by a codeposition method at a large incident angle and subsequent annealing. The fabrication configuration of the codeposition process is shown in Figure 1a. First, a hexagonally close-packed SiO<sub>2</sub> nanosphere monolayer was assembled by an air/water interface method.<sup>24</sup> Then, the monolayer-coated substrates were loaded in a custom-built dual-source electron deposition system. Ag and Fe<sub>3</sub>O<sub>4</sub> were deposited simultaneously onto the SiO<sub>2</sub> nanospheres with an incident angle of 86°. NRs would grow on the SiO<sub>2</sub> nanospheres due to the self-shadow effect and self-alignment (Figure 1b).<sup>25</sup> Then, the as-deposited samples were annealed in N<sub>2</sub>/EtOH with 350 °C and 1 h to tune the Fe<sub>2</sub>O<sub>3</sub> to Fe<sub>3</sub>O<sub>4</sub>, obtaining composite Ag/Fe<sub>3</sub>O<sub>4</sub> NRs (Figure 1c). Porous Fe<sub>3</sub>O<sub>4</sub> NRs can be achieved by etching the composite Ag/Fe<sub>3</sub>O<sub>4</sub> NRs in KCN to remove Ag (Figure 1d).

Figure 1e and 1h shows the SEM images of the samples after codeposition. The diameter of the SiO<sub>2</sub> nanosphere was 500 nm, and the ratio of the deposition rate of Ag and Fe<sub>3</sub>O<sub>4</sub> was 1:2. Clearly, all of the NRs were formed on top of the SiO<sub>2</sub> nanospheres and tilted with respect to the surface normal. The length (L) and diameter (D) of the NRs were 1.40  $\pm$  0.05  $\mu$ m and  $400 \pm 20$  nm, respectively. There were visible Ag NPs on the surface of NRs (indicated by the red arrows in Figure 1h) whose average diameter was determined to be  $100 \pm 7$  nm. The size of the inner Ag NPs was inferred to be <100 nm. The elements O, Ag, and Fe were identified in the as-deposited samples by energy-dispersive X-ray spectroscopy (EDS) whose atom ratio was 13:4:5. Typical X-ray diffraction (XRD) patterns of Ag are shown with the black line in Figure 1k, indicating the formation of crystals in the NRs. No other XRD patterns of the as-deposited samples appeared because Ag occupied the surface and covered the XRD peaks of other crystals. We note that Fe<sub>2</sub>O<sub>3</sub> may exist in the as-deposited samples. After annealing, as shown in Figure 1f and 1i, the overall L and D of the NRs remained the same, while more Ag

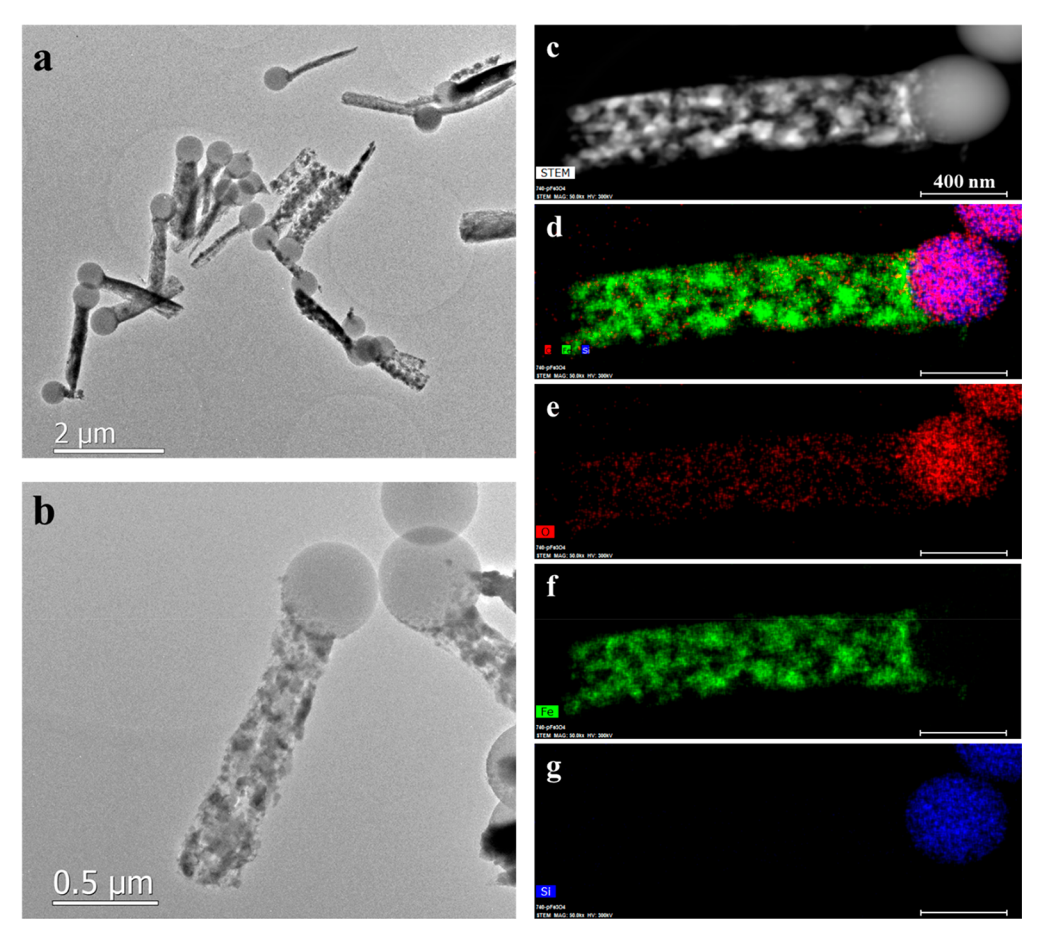


Figure 2. (a, b) Bright-field TEM images of the porous Fe<sub>3</sub>O<sub>4</sub> NRs. (c) Dark-field TEM image of a single porous Fe<sub>3</sub>O<sub>4</sub> NR. EDS mapping of (d) O/Fe/Si, (e) O, (f) Fe, and (g) Si.

NPs appeared to be segregated to the surface of the NRs with a similar diameter (indicated by the red arrows in Figure 1i). The atom ratio of O, Ag, and Fe was 20:3:5. The increase of the O atom ratio and decrease of the Ag atom ratio were due to Ag being annealed to larger NPs and more Fe<sub>3</sub>O<sub>4</sub> exposed. In the XRD pattern (red curve in Figure 1k), all of the Agrelated crystal peaks became more prominent and extra peaks from Fe<sub>3</sub>O<sub>4</sub> (511) and Fe<sub>3</sub>O<sub>4</sub> (422) appeared, indicating the formation of Fe<sub>3</sub>O<sub>4</sub> nanocrystals, i.e., the as-deposited NRs were transformed to Fe<sub>3</sub>O<sub>4</sub> and composite Ag/Fe<sub>3</sub>O<sub>4</sub> NRs. The SEM images of the samples after being etched for 50 min are shown in Figure 1g and 1j, revealing that the surface of the NRs became rather rough and exhibited clear porosity, and the NPs on the surface disappeared. The L and D of the NRs still remained as 1.40  $\pm$  0.05  $\mu$ m and 400  $\pm$  20 nm, respectively. The atom ratio of Ag in EDX became zero, and no XRD peaks of the Ag crystals were observed (blue curve in Figure 1k), indicating that the Ag in the composite NRs was completely removed. The Fe:O atomic ratio was still 5:20, indicating that Fe<sub>3</sub>O<sub>4</sub> would not be lost in the etching process. In the XRD pattern multiple Fe<sub>3</sub>O<sub>4</sub> crystalline peaks at (220), (311), (400), and (440) became distinct. However, the crystalline quality of the resulting porous Fe<sub>3</sub>O<sub>4</sub> NRs was not high since the relative intensities of these crystal peaks were low and the XRD pattern was noisy, which may be due to the fact that the etching destroyed the crystal structure and generated much smaller Fe<sub>3</sub>O<sub>4</sub> crystals or amorphous Fe<sub>3</sub>O<sub>4</sub> NRs. Further annealing could improve the crystal quality of the porous Fe<sub>3</sub>O<sub>4</sub> NRs. The roughness and porosity can be controlled by

the  ${\rm Ag/Fe_3O_4}$  ratio and etching duration. The diameter and length of the NRs depend on the sphere size and deposition surface mass, respectively, which both can vary from below 100 nm to several micrometers.  $^{26,27}$ 

The quality of the porous Fe<sub>3</sub>O<sub>4</sub> NRs was further examined by high-resolution SEM and element mapping as shown in Figure 2. To obtain these SEM images, the NRs were first sonicated in EtOH and then dispensed on the TEM grid. Figure 2a and 2b shows that even though the NRs became highly porous, they were still attached to the silica nanospheres. All of the Fe<sub>3</sub>O<sub>4</sub> portions of NRs showed dense pinholes. EDS mappings showed a well-defined element distribution (Figure 2c-g), where O appeared in both the NRs and the nanospheres, Fe was only observed in the NRs, and Si only existed in the nanospheres. Again, the distribution of Fe showed clear porosity.

Clearly by changing the nanosphere and relative deposition ratio of Ag and Fe $_3O_4$ , one can fabricate different composite Ag/Fe $_3O_4$  and porous Fe $_3O_4$  NRs. For example, using 800 nm nanospheres and a deposition rate ratio of 1:1, composite Ag/Fe $_3O_4$  NRs with different diameters ( $\sim$ 600 nm) and composition as well as porous Fe $_3O_4$  NRs with different pore sizes were fabricated (see Figure S1 in the Supporting Information (SI)), demonstrating the generality of the fabrication method for varied composite and porous NRs. These NRs were fabricated by a physical deposition process with no mask and avoiding uncontrolled chemical reactions. Thus, this fabrication method is versatile, inexpensive, and capable of patterning large areas in parallel at low cost. It can

be applied with only less sophisticated equipment yet with good control of the main structural parameters.

The magnetization property of the porous  $Fe_3O_4$  NRs shown in Figure 1g was measured by a vibrating sample magnetometer (VSM) at room temperature, and the magnetic hysteresis loop is shown in Figure 3. A significant hysteresis

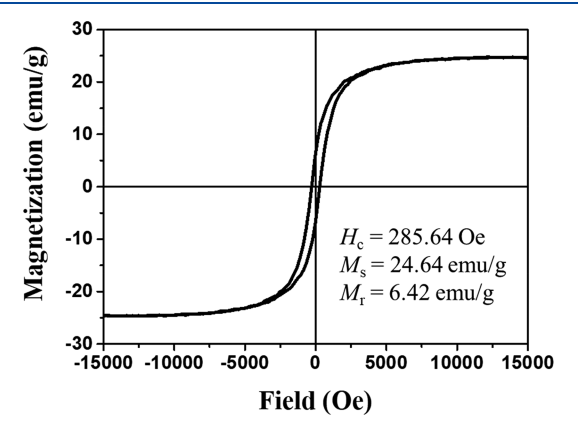
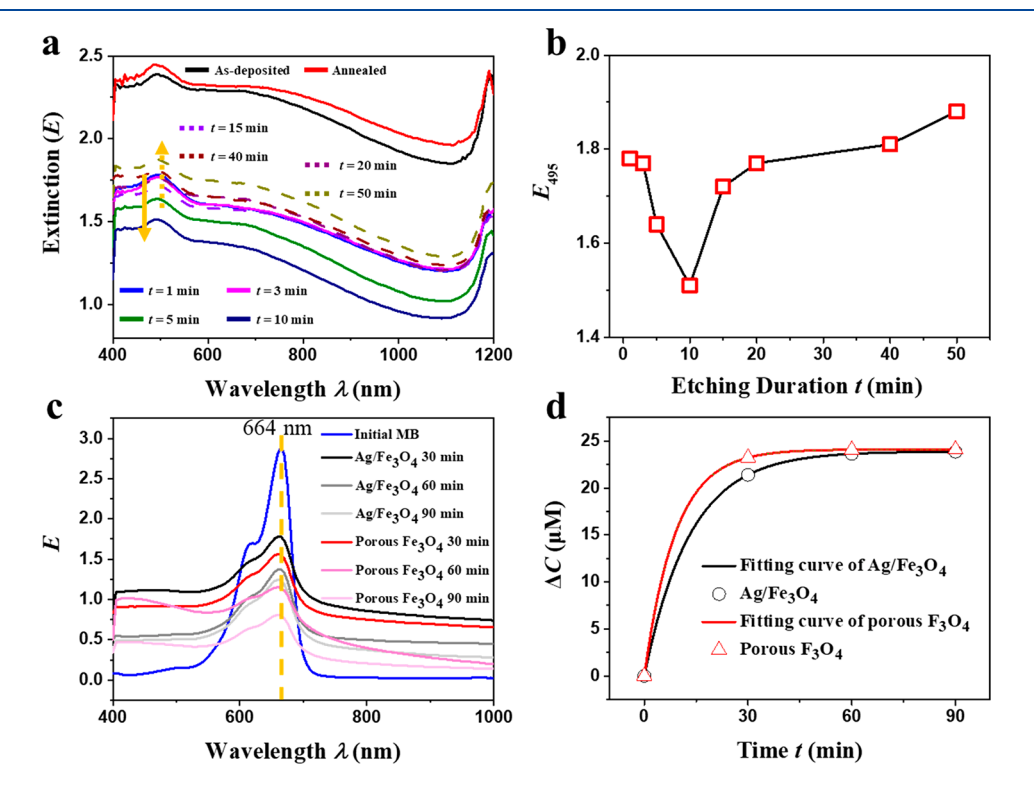


Figure 3. Magnetization hysteresis loop of porous  $Fe_3O_4$  measured at room temperature.

loop in the M-H curve indicated the ferromagnetic behavior of the porous Fe<sub>3</sub>O<sub>4</sub> NRs. The saturation magnetization ( $M_s$ ), coercivity ( $H_c$ ), and retentivity ( $M_r$ ) were obtained to be 24.64 emu/g, 285.64 Oe, and 6.42 emu/g, respectively. The measured value was much smaller than the theoretical one for bulk Fe<sub>3</sub>O<sub>4</sub> (92 emu/g) at room temperature.<sup>28</sup> The difference can be attributed to the low crystallization and possible size effect on magnetization which significantly

lowered the magnetic performance of the porous  $Fe_3O_4$  NRs.  $^{6,19,29,30}$  To increase the ferromagnetism, further annealing may be applied for the larger crystal structure of  $Fe_3O_4$ . The ferromagnetic behavior makes the NRs easy to be manipulated and collected and could have potential applications as a drug carrier, for biolabeling, for photocatalysis, etc.

The optical extinction (E) spectra of the as-deposited, annealed, and etched (different durations) NRs shown in Figure 1 are plotted in Figure 4a. The *E* spectra for both the asdeposited and the annealed samples showed broad-band high extinction across the visible to near-infrared wavelength region. Such broad and high extinction spectra are due to the absorption of light by localized surface plasmon resonance (LSPR) of various sized Ag NPs and the scattering of the Ag NPs as well as the NRs. The E of the annealed sample was slightly higher than that of the as-deposited sample since due to the annealing more Ag NPs were formed and segregated onto the surface, leading to stronger LSPR absorption and NP scattering.<sup>31</sup> However, the E spectra of the annealed sample versus etching duration t showed a very interesting relationship: the overall E value first decreased with t and then increased later. A quantitative trend can be revealed when the E at  $\lambda = 495$  nm  $(E_{495})$  was plotted as a function of t as shown in Figure 4b. In the beginning,  $E_{495}$  started at 1.78 at t = 0 min, dropped monotonically with etching duration, and reached a minimum of 1.51 at t = 10 min. At t > 10 min,  $E_{495}$  increased monotonically with t and restored to 1.88 at t = 50 min when Ag was completely removed. The decrease of  $E_{495}$  before t = 10min was due to Ag etching, i.e., that both the size of the Ag NPs and the amount of Ag materials became less in the NRs and the absorption due to LSPR and the scattering due to the



**Figure 4.** (a) *E* of the as-deposited, annealed, and etched samples for t = 1, 3, 5, 10, 15, 40, and 50 min. (b) Plot of  $E_{495}$  with the etching duration. (c) *E* of the initial MB solution, MB solution with composite Ag/Fe<sub>3</sub>O<sub>4</sub> NRs for t = 30, 60, and 90 min, and MB solution with porous Fe<sub>3</sub>O<sub>4</sub> NRs for t = 30, 60, and 90 min. (d) Plot and curve fitting of  $\Delta C$  as a function of the adsorption time.

NPs became less and less significant. However, at t > 10 min, though there were still Ag NPs, compared to the pore size formed in the NRs, the absorption and scattering due to the Ag NPs became negligible; rather the scattering and light trapping by the pores became more and more significant, which made the values of E higher. However, the E of the porous Fe<sub>3</sub>O<sub>4</sub> NRs was much lower than that of the annealed composite Ag/Fe<sub>3</sub>O<sub>4</sub> NRs, demonstrating that the LSPR effect of the Ag NPs played a more significant role in determining the optical property compared to the light trapping and scattering by the pores. The composite Ag/Fe<sub>3</sub>O<sub>4</sub> NRs and porous Fe<sub>3</sub>O<sub>4</sub> NRs with tunable optical properties indicated the promising use in light trapping and optics.

The composite and porous NRs are ideal materials for dye adsorption, which was investigated by methylene blue (MB). Figure 4c shows the initial and time-dependent E spectra of the MB solution for composite  $Ag/Fe_3O_4$  NRs ( $E_{composite}$ ) and porous  $Fe_3O_4$  NRs ( $E_{porous}$ ). The E spectrum for MB showed a distinct peak at  $\lambda = 664$  nm. When the composite Ag/Fe<sub>3</sub>O<sub>4</sub> NRs and porous Fe<sub>3</sub>O<sub>4</sub> NRs were added into the initial MB solution and as t increased, both  $E_{\text{composite}}$  and  $E_{\text{porous}}$  decreased while  $E_{\text{composite}}$  was always higher than  $E_{\text{porous}}$ . The concentration loss ( $\Delta C$ ) of MB with t was calculated by tracking the change of  $E_{\text{composite}}$  and  $E_{\text{porous}}$  at  $\lambda = 664$  nm, as shown in Figure 4d. The calculation was based on the calibration curve obtained from UV-vis extinction spectra of MB aqueous solutions with known concentrations using E at  $\lambda = 664$  nm (Figure S2).  $\Delta C_{\text{composite}}$  and  $\Delta C_{\text{porous}}$  increased monotonically with t and reached a saturation value during t = 60-90 min. In this process,  $\Delta C_{
m porous}$  remained larger than  $\Delta C_{
m composite}$ , indicating that MB was adsorbed faster to the porous Fe<sub>3</sub>O<sub>4</sub> NRs than to the composite Ag/Fe<sub>3</sub>O<sub>4</sub> NRs. Such a trend is consistent with the molecular adsorption kinetics on a surface and can be fitted by the following kinetic equation

$$\Delta C = \Delta C_s [1 - e^{-k(t-t_0)}]$$

where  $\Delta C_s$  is the saturation concentration loss, k is the adsorption rate constant, and  $t_0$  is the initial time of adsorption. From Figure 4d, the adsorption rate constants, k, were determined to be 0.075 and 0.111 min<sup>-1</sup> for composite Ag/Fe<sub>3</sub>O<sub>4</sub> NRs and porous Fe<sub>3</sub>O<sub>4</sub> NRs, respectively. Clearly, the MB adsorption rate to porous Fe<sub>3</sub>O<sub>4</sub> NRs is significantly larger (~1.5-fold) than that of the composite Ag/Fe<sub>3</sub>O<sub>4</sub> NRs. The fast adsorption and large loading capability with the ferromagnetism make the porous Fe<sub>3</sub>O<sub>4</sub> NRs promising drug carriers for therapeutic agents.

# CONCLUSIONS

In summary, composite  $Ag/Fe_3O_4$  and porous  $Fe_3O_4$  NRs with ferromagnetism, tunable optical properties, and strong carrier capability were fabricated by a simple and efficient oblique angle codeposition technique. The structural parameters can be better controlled than those prepared by the conventional chemical processes. Moreover, more materials can be doped with  $Fe_3O_4$  through this fabrication method, forming functional composite materials. The composition ratio also can be easily tuned by the deposition process. Simultaneously, the porosity of the  $Fe_3O_4$  NRs can be controlled by the composition ratio. The composite  $Ag/Fe_3O_4$  and porous  $Fe_3O_4$  NRs with improved performance and easy magnetic manipulation are believed to offer great potential for biotechnology, biosensing, catalysis, magnetic fluids, separation

techniques, energy storage, and environmental modification. We have concentrated here on the Ag-doped  ${\rm Fe_3O_4}$  NRs but should mention that this fabrication method also provided the opportunity for pursuing better performance for composite  ${\rm Fe_3O_4}$  NRs with different materials. The materials with unique properties will lend the  ${\rm Fe_3O_4}$ -based NPs more functionalities and applications.

## ASSOCIATED CONTENT

# Supporting Information

The Supporting Information is available free of charge at https://pubs.acs.org/doi/10.1021/acs.jpcc.1c02843.

SEM images of different nanorods, and calibration curve of the extinction spectra of MB solution (PDF)

#### AUTHOR INFORMATION

## **Corresponding Author**

Bin Ai — School of Microelectronics and Communication Engineering, Chongqing University, Chongqing 400044, P.R. China; Chongqing Key Laboratory of Bioperception & Intelligent Information Processing, Chongqing 400044, P.R. China; ⊚ orcid.org/0000-0002-0502-9166; Email: binai@ cqu.edu.cn

#### **Authors**

Weijie Huang — Department of Physics and Astronomy, University of Georgia, Athens, Georgia 30602, United States Xibo Li — Department of Physics and Astronomy, University of Georgia, Athens, Georgia 30602, United States Yiping Zhao — Department of Physics and Astronomy, University of Georgia, Athens, Georgia 30602, United States;

orcid.org/0000-0002-3710-4159

Complete contact information is available at: https://pubs.acs.org/10.1021/acs.jpcc.1c02843

## **Author Contributions**

W.H. and X.L. conducted the experiments. B.A. and Y.Z. performed data analysis. B.A. organized and wrote the manuscript. All authors contributed to the revision and final discussion of the manuscript.

#### Notes

The authors declare no competing financial interest.

## ACKNOWLEDGMENTS

W.H. and Y.Z. were partially supported by the National Science Foundation under Grant No. ECCS-1808271. B.A. was partially supported by Natural Science Foundation of Chongqing of China (cstc2020jcyj-msxmX0614), Open Foundation of Defense Key Disciplines Lab of Novel Micronano Devices and System Technology, and Open Foundation of Chongqing University Key Lab of Optoelectronic Materials and Engineering.

## REFERENCES

- (1) Wu, W.; He, Q.; Jiang, C. Magnetic Iron Oxide Nanoparticles: Synthesis and Surface Functionalization Strategies. *Nanoscale Res. Lett.* **2008**. 3, 397.
- (2) Vallabani, N. V. S.; Singh, S. Recent Advances and Future Prospects of Iron Oxide Nanoparticles in Biomedicine and Diagnostics. 3 Biotechnol. 2018, 8, 279.

- (3) Wu, W.; Jiang, C. Z.; Roy, V. A. L. Designed Synthesis and Surface Engineering Strategies of Magnetic Iron Oxide Nanoparticles for Biomedical Applications. *Nanoscale* **2016**, *8*, 19421–19474.
- (4) Hu, Y.; Mignani, S.; Majoral, J. P.; Shen, M. W.; Shi, X. Y. Construction of Iron Oxide Nanoparticle-Based Hybrid Platforms for Tumor Imaging and Therapy. *Chem. Soc. Rev.* **2018**, *47*, 1874–1900.
- (5) Urbanova, V.; Magro, M.; Gedanken, A.; Baratella, D.; Vianello, F.; Zboril, R. Nanocrystalline Iron Oxides, Composites, and Related Materials as a Platform for Electrochemical, Magnetic, and Chemical Biosensors. *Chem. Mater.* **2014**, *26*, 6653–6673.
- (6) Li, Y.; Zhao, J. W.; You, W. L.; Cheng, D. H.; Ni, W. H. Gold Nanorod@Iron Oxide Core-Shell Heterostructures: Synthesis, Characterization, and Photocatalytic Performance. *Nanoscale* **2017**, *9*, 3925–3933.
- (7) Han, X.; Lee, H. K.; Lim, W. C.; Lee, Y. H.; Phan-Quang, G. C.; Phang, I. Y.; Ling, X. Y. Spinning Liquid Marble and Its Dual Applications as Microcentrifuge and Miniature Localized Viscometer. *ACS Appl. Mater. Interfaces* **2016**, *8*, 23941–23946.
- (8) Dias, A. M. G. C.; Hussain, A.; Marcos, A. S.; Roque, A. C. A. A Biotechnological Perspective on the Application of Iron Oxide Magnetic Colloids Modified with Polysaccharides. *Biotechnol. Adv.* 2011, 29, 142–155.
- (9) Zeng, Y.; Yu, M.; Meng, Y.; Fang, P.; Lu, X.; Tong, Y. Iron-Based Supercapacitor Electrodes: Advances and Challenges. *Adv. Energy Mater.* **2016**, *6*, 1601053.
- (10) Li, Y. Z.; Liang, T.; Wang, R.; He, B. B.; Gong, Y. S.; Wang, H. W. Encapsulation of  $Fe_3O_4$  between Copper Nanorod and Thin  $TiO_2$  Film by Ald for Lithium-Ion Capacitors. *ACS Appl. Mater. Interfaces* **2019**, *11*, 19115–19122.
- (11) Xu, P.; et al. Use of Iron Oxide Nanomaterials in Wastewater Treatment: A Review. Sci. Total Environ. 2012, 424, 1–10.
- (12) Liu, B.; Zhang, W.; Zhang, D.; Yang, X. Facile Method for Large Scale Synthesis of Magnetic Inorganic-Organic Hybrid Anisotropic Janus Particles. *J. Colloid Interface Sci.* **2012**, 385, 34–40.
- (13) Cao, S.-W.; Zhu, Y.-J.; Ma, M.-Y.; Li, L.; Zhang, L. Hierarchically Nanostructured Magnetic Hollow Spheres of Fe $_3$ O $_4$ : Preparation and Potential Application in Drug Delivery. *J. Phys. Chem. C* **2008**, *112*, 1851–1856.
- (14) Xiong, Q. Q.; Lu, Y.; Wang, X. L.; Gu, C. D.; Qiao, Y. Q.; Tu, J. P. Improved Electrochemical Performance of Porous  $Fe_3O_4/Carbon$  Core/Shell Nanorods as an Anode for Lithium-Ion Batteries. *J. Alloys Compd.* **2012**, *536*, 219–225.
- (15) Zheng, J.; Dong, Y.; Wang, W.; Ma, Y.; Hu, J.; Chen, X.; Chen, X. In Situ Loading of Gold Nanoparticles on Fe<sub>3</sub>O<sub>4</sub>@SiO<sub>2</sub> Magnetic Nanocomposites and Their High Catalytic Activity. *Nanoscale* **2013**, *5*, 4894–4901.
- (16) Li, J.; Zheng, L.; Cai, H.; Sun, W.; Shen, M.; Zhang, G.; Shi, X. Facile One-Pot Synthesis of Fe<sub>3</sub>O<sub>4</sub>@Au Composite Nanoparticles for Dual-Mode Mr/Ct Imaging Applications. *ACS Appl. Mater. Interfaces* **2013**, *5*, 10357–10366.
- (17) Wang, C.; Daimon, H.; Sun, S. Dumbbell-Like Pt–Fe3o4 Nanoparticles and Their Enhanced Catalysis for Oxygen Reduction Reaction. *Nano Lett.* **2009**, *9*, 1493–1496.
- (18) Fu, C.; He, D. W.; Wang, Y. S.; Zhao, X. Facile Synthesis of Porous Fe<sub>3</sub>O<sub>4</sub>@C Core/Shell Nanorod/Graphene for Improving Microwave Absorption Properties. RSC Adv. 2018, 8, 15358–15365.
- (19) Chen, Y. J.; Xiao, G.; Wang, T. S.; Ouyang, Q. Y.; Qi, L. H.; Ma, Y.; Gao, P.; Zhu, C. L.; Cao, M. S.; Jin, H. B. Porous Fe<sub>3</sub>O<sub>4</sub>/Carbon Core/Shell Nanorods: Synthesis and Electromagnetic Properties. *J. Phys. Chem. C* **2011**, *115*, 13603–13608.
- (20) Jazirehpour, M.; Seyyed Ebrahimi, S.A. Carbothermally Synthesized Core-Shell Carbon-Magnetite Porous Nanorods for High-Performance Electromagnetic Wave Absorption and the Effect of the Heterointerface. *J. Alloys Compd.* **2015**, *639*, 280–288.
- (21) Roh, Y.; Vali, H.; Phelps, T. J.; Moon, J. W. Extracellular Synthesis of Magnetite and Metal-Substituted Magnetite Nanoparticles. *J. Nanosci. Nanotechnol.* **2006**, *6*, 3517–3520.
- (22) Bharde, A. A.; Parikh, R. Y.; Baidakova, M.; Jouen, S.; Hannoyer, B.; Enoki, T.; Prasad, B. L. V.; Shouche, Y. S.; Ogale, S.;

- Sastry, M. Bacteria-Mediated Precursor-Dependent Biosynthesis of Superparamagnetic Iron Oxide and Iron Sulfide Nanoparticles. *Langmuir* **2008**, *24*, 5787–5794.
- (23) Larson, S.; Carlson, D.; Ai, B.; Zhao, Y. P. The Extraordinary Optical Transmission and Sensing Properties of Ag/Ti Composite Nanohole Arrays. *Phys. Chem. Chem. Phys.* **2019**, 21, 3771–3780.
- (24) Ingram, W.; He, Y. Z.; Stone, K.; Dennis, W. M.; Ye, D. X.; Zhao, Y. P. Tuning the Plasmonic Properties of Silver Nanopatterns Fabricated by Shadow Nanosphere Lithography. *Nanotechnology* **2016**, *27*, 385301.
- (25) Vankranenburg, H.; Lodder, C. Tailoring Growth and Local Composition by Oblique-Incidence Deposition a Review and New Experimental-Data. *Mater. Sci. Eng., R* **1994**, *11*, 295–354.
- (26) Satoshi, K.; Zhang, Z.-J.; Shi, J.; Yoshio, N. Characterization of CoPt Nanowire Fabricated by Glancing Angle Deposition. *Chin. Phys.* B **2015**, 24, 056201.
- (27) Dolatshahi-Pirouz, A.; Sutherland, D. S.; Foss, M.; Besenbacher, F. Growth Characteristics of Inclined Columns Produced by Glancing Angle Deposition (Glad) and Colloidal Lithography. *Appl. Surf. Sci.* **2011**, 257, 2226–2230.
- (28) Xi, G.; Wang, C.; Wang, X. The Oriented Self-Assembly of Magnetic Fe3o4 Nanoparticles into Monodisperse Microspheres and Their Use as Substrates in the Formation of Fe3o4 Nanorods. *Eur. J. Inorg. Chem.* **2008**, 2008, 425–431.
- (29) Xuan, S.; Wang, Y.-X. J.; Yu, J. C.; Cham-Fai Leung, K. Tuning the Grain Size and Particle Size of Superparamagnetic  $Fe_3O_4$  Microparticles. *Chem. Mater.* **2009**, *21*, 5079–5087.
- (30) He, X.; Zhong, W.; Au, C.-T.; Du, Y. Size Dependence of the Magnetic Properties of Ni Nanoparticles Prepared by Thermal Decomposition Method. *Nanoscale Res. Lett.* **2013**, *8*, 446.
- (31) Homola, J. Surface Plasmon Resonance Sensors for Detection of Chemical and Biological Species. *Chem. Rev.* **2008**, *108*, 462–493.